



This is a repository copy of *Energy repartition and entropy generation across the Earth's bow shock: MMS observations*.

White Rose Research Online URL for this paper:

<https://eprints.whiterose.ac.uk/202018/>

Version: Published Version

Article:

Agapitov, O.V. orcid.org/0000-0001-6427-1596, Krasnoselskikh, V. orcid.org/0000-0002-6809-6219, Balikhin, M. orcid.org/0000-0002-8110-5626 et al. (3 more authors) (2023) Energy repartition and entropy generation across the Earth's bow shock: MMS observations. *The Astrophysical Journal*, 952 (2). 154. ISSN 0004-637X

<https://doi.org/10.3847/1538-4357/acdb7b>

Reuse

This article is distributed under the terms of the Creative Commons Attribution (CC BY) licence. This licence allows you to distribute, remix, tweak, and build upon the work, even commercially, as long as you credit the authors for the original work. More information and the full terms of the licence here:

<https://creativecommons.org/licenses/>

Takedown

If you consider content in White Rose Research Online to be in breach of UK law, please notify us by emailing eprints@whiterose.ac.uk including the URL of the record and the reason for the withdrawal request.



eprints@whiterose.ac.uk
<https://eprints.whiterose.ac.uk/>



Energy Repartition and Entropy Generation across the Earth's Bow Shock: MMS Observations

O. V. Agapitov^{1,2}, V. Krasnoselskikh^{1,3}, M. Balikhin⁴, J. W. Bonnell¹, F. S. Mozer¹, and L. Avanov⁵¹Space Sciences Laboratory, University of California, Berkeley, CA 94720, USA; agapitov@ssl.berkeley.edu²Astronomy and Space Physics Department, National Taras Shevchenko University of Kyiv, Kyiv, Ukraine³LPC2E-University of Orleans, Orleans, France⁴University of Sheffield, Sheffield, UK⁵NASA GSFC, Greenbelt, MD 20771, USA

Received 2023 March 14; revised 2023 May 15; accepted 2023 May 28; published 2023 July 26

Abstract

The evolution of plasma entropy and the process of plasma energy redistribution at the collisionless plasma shock front are evaluated based on the high temporal resolution data from the four Magnetospheric Multiscale spacecraft during the crossing of the terrestrial bow shock. The ion distribution function has been separated into the populations with different characteristic behaviors in the vicinity of the shock: the upstream core population, the reflected ions, the gyrating ions, the ions trapped in the vicinity of the shock, and the downstream core population. The values of ion and electron moments (density, bulk velocity, and temperature) have been determined separately for these populations. It is shown that the solar wind core population bulk velocity slows down mainly in the ramp with the electrostatic potential increase but not in the foot region as it was supposed. The reflected ion population determines the foot region properties, so the proton temperature peak in the foot region is an effect of the relative motion of the different ion populations, rather than an actual increase in the thermal speed of any of the ion population. The ion entropy evaluated showed a significant increase across the shock: the enhancement of the ion entropy occurs in the foot of the shock front and at the ramp, where the reflected ions are emerging in addition to the upstream solar wind ions, the anisotropy growing to generate the bursts of ion-scale electrostatic waves. The entropy of electrons across the shock does not show a significant change: electron heating goes almost adiabatically.

Unified Astronomy Thesaurus concepts: [Solar wind \(1534\)](#); [Planetary bow shocks \(1246\)](#)

1. Introduction

Collisionless shocks (CSs) are ubiquitous in space plasma and astrophysical systems. They play an essential role in the interaction of the solar wind with the planets, and they are supposed to play a crucial role in fundamental problems of astrophysics in the acceleration of cosmic rays (Axford et al. 1977; Krymskii 1977; Bell 1978). CSs arise in astrophysical systems where a supersonic flow interacts with an obstacle or two high-speed flows of different origins penetrate one another. CSs form near many astrophysical objects such as supernova remnants, plasma jets, binary objects, and ordinary stars. Despite a great variety of CSs in the universe currently, only CSs in the solar system can be probed using in situ observations. Kennel et al. (1985) noted that plasma density, temperature, and magnetic field in the hot interstellar medium are similar to those in the solar wind, and the Mach numbers of supernova shocks at the phase when they accelerate the most cosmic rays are similar to those of solar wind shocks. Thus, the study of terrestrial and heliospheric CS allows one to quantify and constrain the physics in both these local CSs, as well as those found in important astrophysical systems.

CSs decelerate the flow from supersonic to subsonic and transform part of the kinetic energy of directed flow motion into thermal energy—thermalization. In gas dynamics, this process inevitably involves particle collisions and the

corresponding thermalization produces entropy. The scale of the transition region in such a process should be larger than the mean free path of particles. In collisionless plasmas, this would mean unrealistic spatial scales, which in the case of the terrestrial bow shock are comparable to the distance from the Sun to Jupiter. The Earth bow shock and other planetary and interplanetary CS are much thinner than this, and so the physics that determines their thickness is quite different than that of CSs. The actual structure of a quasi-perpendicular CS is more complicated than an abrupt transition from upstream to downstream conditions (Krasnoselskikh et al. 2013; Leroy et al. 1982). The conventional notion of the quasi-perpendicular Earth's bow shock (the CS standing in the magnetosphere frame) includes several elements: the foreshock region, the foot, the ramp region, the overshoot and undershoot regions, and the magnetosheath region separating the magnetopause from the shock. For supercritical CSs (with a Mach number typically greater than 3), the ion reflection presumably determines the main energy conversion (Schwartz et al. 2021, 2022), so the shock rump and foot with a major change in the parameters is of special importance and is widely considered as the shock front (Hanson et al. 2019).

The simplified MHD description of CSs determines the main asymptotic characteristics (density, velocity, pressure, temperature, etc.) of the downstream flow from the known parameters of the upstream flow through conservation of mass, momentum, energy flux, and equation of state across a *black box* transition region (see the following for details: Kennel et al. (1985)). This model assumes that all the relaxation processes occur inside this transition, and the



Original content from this work may be used under the terms of the [Creative Commons Attribution 4.0 licence](#). Any further distribution of this work must maintain attribution to the author(s) and the title of the work, journal citation and DOI.

downstream flow is in thermal equilibrium defined by Rankine–Hugoniot relations representing conservation laws for stationary flows. This model assumes that the modification of the flow after crossing the shock front is supposed to be irreversible, and thus that the shock naturally produces an increase in entropy (Birn et al. 2004; Liu et al. 2007). However, even in the magnetosheath region, the asymptotic conditions determined by Rankine–Hugoniot conditions are not fully satisfied—in other words, the state of the plasma may be stable but not obligatorily corresponding to the final downstream thermal equilibrium. Comparing the plasma parameters in the downstream regions of collisional and CSs, one may conclude that CSs cannot provide full thermalization, i.e., the downstream flow cannot reach new thermal equilibrium corresponding to the state with increased entropy. According to the Boltzmann equation for collisional plasma the full time derivative of the distribution function df/dt is equal to the collisional term (Stosszahlansatz). This term describes the effects of collisions and leads to the irreversible evolution toward thermodynamic equilibrium. In the case of collisionless plasmas, and if we follow the particular region in the phase space in accordance with Lowville’s theorem, the phase space density remains constant along that region’s trajectory through the phase space. Therefore, if we follow the same population of particles, the corresponding entropy should remain constant. Observations from heliospheric low Mach number shocks have shown that electrons often are not heated much beyond the adiabatic compression and heating associated with the macroscopic structure (change in $|B|$, cross-shock E field, etc.) of the shock (Bame et al. 1979). However, there have been instances where a given CS produces an increase in entropy, manifested as super-adiabatic heating of ion and/or electron populations (Sckopke et al. 1990; Sckopke 1995; Parks et al. 2012; Lindberg et al. 2022). In an MHD description of the plasma, it is supposed that the different populations of particles are in thermal equilibrium. In that case, entropy is a function of the total density and pressure of the plasma (the fluid approximation). In a more general case, the kinetic Boltzmann definition of entropy as defined above can be estimated from plasma distribution functions. For the terrestrial bow shock and other CSs, computing the kinetic Boltzmann entropy requires rapid measurements of the detailed distribution functions of particles (Parks et al. 2012; Lindberg et al. 2022). Parks et al. (2012) first reported the dynamics of entropy per particle (density of entropy) and showed that it does increase across the Earth’s bow shock based on the data from Cluster. With one-point measurements, Parks et al. (2012) proposed the concept of entropy density: $\sum p_i \ln p_i$ estimated at a point in space, where $p_i = f_i \Delta^3 v_i / N$ (i is for each of the velocity bins in the three-dimensional velocity space, and N is the particle number in the space volume) normalized so that $\sum p_i = 1$ (Montgomery & Tidman 1964). This approach allows estimating the plasma entropy in the velocity space from particle detector measurements of the flux in the set of energy channels and the full solid angle. Observations of electron heating at the Earth’s bow shock show that electrons are in most cases heated to lower temperatures than the ions (Schwartz et al. 1988), with a Mach number dependence that suggests that there is an inverse correlation between Mach

number and electron-ion temperature ratio suggesting almost adiabatic heating of electrons (Vink et al. 2015). To explore the source of this correlation, Park et al. (2015) studied the particle energization at a CS in a particle-in-cell (PIC) numerical system and found that the fluctuating electromagnetic fields are necessary for the creation of the entropy density throughout the downstream region. The detailed processes leading to entropy changes across the shock were then investigated in PIC plasma models of plasma shocks (Yang et al. 2014; Guo et al. 2017, 2018) and reconnection systems (Liang et al. 2019, Du et al. 2020). Guo et al. (2017, 2018) showed that while most of the electron heating in low Mach number shocks is adiabatic, the irreversible electron heating indicated by the enhancement in entropy can also be observed. Two basic ingredients were identified as necessary for the production of entropy: (1) a temperature anisotropy, induced by field amplification coupled to adiabatic invariance; and (2) a mechanism to break the particles’ adiabatic invariance itself (Guo et al. 2017, 2018). To account for this production of entropy, early models of CS included the concept of *anomalous collisions*, as first formulated by Sagdeev (1966) and Galeev (1976). According to this concept, the interactions of upstream plasma particles with waves generated by various plasma instabilities within the shock front play the role of collisions in ordinary collisional gas dynamic shocks. The question of whether anomalous collisions play a key role in a terrestrial bow and lead to irreversibility across the shock front remains open. It is worth noting that entropy is presumably the most precise measurement in the characterization of the process of the transformation of directed energy into thermal, but it is not widely used in practice, and the direct estimation of the change in entropy using the unprecedentedly high-time resolution Magnetospheric Multiscale (MMS) plasma measurements allows to clarify this problem for the terrestrial bow shock.

In this paper, we demonstrate the valuable insights gained by applying the concept of entropy density and its changes across the terrestrial bow shock to determine what processes contribute significantly to irreversible changes in the plasma distributions, and where those processes occur within the shock structure. To do that, we first use the high-cadence, high-resolution MMS particle data to distinguish the proton populations with different characteristic dynamics across the Earth’s bow shock (core upstream, reflected, core downstream). We then evaluate the partial moments (density, velocity, temperature, entropy density) of these populations to determine which vary and in what ways. We then use those observations, along with the detailed electromagnetic field measurements on MMS, to determine the factors responsible for producing entropy in the CS.

Dynamics of the particles’ distribution functions during a bow shock crossing by MMS on 2017 November 2.

Hereafter, we discuss a high-beta, quasi-perpendicular CS making use of multipoint observations from the MMS constellation (Burch et al. 2016). The MMS mission makes plasma measurements with a high sampling rate and energy/angle resolution that can resolve the dynamics of the particle distribution across the shock front contributed by the different particle populations. MMS is a four-spacecraft constellation in a tetrahedral formation with typical separation distances of tens

of kilometers (Fuselier et al. 2016). The Fast Plasma Investigation (FPI) suite on board the MMS spacecraft consists of four dual electrons and four dual ion electrostatic spectrometers (Pollock et al. 2016). The FPI has a high rate of electron and proton distribution function measurements producing the full solid angle flux distribution with 30 S/s for electrons and 3 S/s for protons (Pollock et al. 2016). It provides measurements of the three-dimensional distribution functions in the energy range from 10–30 keV/q on each spacecraft. Using electrostatic field-of-view deflection, the eight spectrometers together provide a 4pi-sr field-of-view with 11°25 sample spacing. The counts corresponding to each bin in the phase space are combined into a sky map, which is a three-dimensional array with 32 energy, 32 azimuth angles, and 16 polar angles. The FPI continuously operates in burst mode throughout the bow shock crossings. The wave instruments on MMS provide rapid measurements of three components of the electric field (Ergun et al. 2016; Lindqvist et al. 2016), three components of the magnetic field from SCM (Le Contel et al. 2016), and three components of the background magnetic field from FGM (Russell et al. 2016).

We consider here the bow shock crossing by the MMS spacecraft on 2015 November 2. Figure 1 shows three components of the magnetic field, ion bulk velocity, ion and electron density, and particle fluxes as measured by the MMS3 spacecraft during this shock front crossing. We notice here the effects of the helium component, which lead to an increase in the estimated proton temperature because of the absence of mass resolution in FPI ion measurements (Halekas et al. 2014). The helium component is seen in ion flux (Figure 1(c)). However, the dynamics of these components are similar across the shock, so we process them together in the following. This bow shock crossing was reported previously by Hanson et al. (2019) (where the measurements in the solar wind were compared with the data from WIND (Wilson et al. 2022)) and Lindberg et al. (2022). The magnetic field, plasma bulk velocity, and plasma density demonstrate the structure typical for a crossing of a high-Mach number quasi-perpendicular CS. The lower energy ions produce a significant foot region with increased density and magnetic field perturbations as can be seen in Figure 1.

The ion density distribution across the shock front is shown in Figure 2 for the far upstream (a), foot (b), ramp (c), and downstream (d) plasma regions of the shock. The solar wind flow is highly localized (beamed) in direction and the energy range in the upstream region (Figures 1(a), (e), and (j)). This focused beamed population remains quite similar in the foot region (highlighted in red in Figure 1(a)). However, there emerge three additional ion populations, namely, the reflected ions (ions reflected from the shock potential similar to the core solar wind population energy), the gyrating ions accelerated in the ramp region of the shock through drift acceleration (see Hanson et al. 2020b), and the downstream ions penetrating to the upstream to the distance about the ion gyroradius (being very similar to the Sun-directed part of the downstream distribution shown in Figure 2(g), (h)). The reflected and downstream populations with different bulk flow velocities significantly complicate the ion plasma distributions through the foot and ramp leading to a biased estimation of plasma bulk velocity and temperature (pressure) (Schwartz et al. 2021, 2022), which makes ion proxies for the evaluation of the shock potential inapplicable (Hanson et al. 2019, Hanson et al. 2020a). In the

ramp, the solar wind ion core population begins to be heated. One can see this as a spreading of the solar wind beam as shown in Figures 2(c) and (g) and an increase of high energy flux as shown in Figure 2(l). The downstream distribution shows the effects of the redistribution of solar wind bulk flow kinetic energy to the thermal energy of more dense plasma with a lower bulk speed. As was described above, because the observed ion populations can be distinguished in phase it is possible to process the parameters of the different populations separately, and more clearly quantify what changes to drift, temperature, and density occur in different parts of phase space.

Calculation of the partial plasma moments (density, bulk speed, and temperature) of the core upstream/downstream and reflected ion populations shows that the reflected population has a density comparable to that of the core solar wind population in the foot region (Figure 3(a)). This affects the direction of the bulk velocity in the foot region: Figure 3(b) presents the revised three components of core ion bulk velocity, and shows that significant changes in the distribution function and slow down of the core population bulk velocity occur only on the ramp of the shock. The parallel and transverse to the background magnetic field temperatures of ions, $T_{i\parallel}$ and $T_{i\perp}$, estimated from the full distribution function are presented in Figure 3(c). The core population is heated across the shock ramp and gains anisotropy of about $T_{i\perp}/T_{i\parallel} \sim 1.5$ –1.8. The electron population is also heated on the shock ramp but much less, from $\sim 15 \pm 1$ to 32 ± 2 eV (Figure 3(e)). Heating of electrons is going isotropically—the parallel and transverse temperatures increase together with similar values in agreement with (Schwartz et al. 2011), who reported that the major electron heating in the ramp region does not manifest any anisotropy. It may be understood as there is intense wave activity in this region and the frequencies are in the ion-acoustic range. The major effect of the interaction of electrons with these low-frequency waves consists of their angular scattering with a very weak energy change. This explains the absence of the anisotropy in this process. The temperatures (here the term *temperature* stands for conventional temperature determined as follows: $T = \frac{m}{3} \langle (v - \langle v \rangle)^2 \rangle > = \frac{m}{3n} \int f(v) (v - \langle v \rangle)^2 dv$, where n is the number density of the corresponding population and $\langle \dots \rangle$ means averaging over the distribution) of the core and reflected ion populations are presented in Figure 3(d). The population separation shows that the temperature peak in the foot is only associated with the reflected ions and the peak values are lower than given by the estimation based on the full distribution. The peak temperatures in the foot are similar to the ion temperatures in the downstream (Figure 3(d)). Thus, the main heating of the core electron population occurs on the shock ramp. Figure 3(g) shows the evolution of the ion anisotropy—the ion anisotropy, $A_i = T_{i\perp}/T_{i\parallel} - 1$, peaks at the ramp and can be unstable for generation of the ion cyclotron waves (the instability threshold is indicated by the red dashed curve). Intense electrostatic waves (with amplitudes up to 100 mV m⁻¹) are observed on the shock ramp (Figures 1(g) and 3(h)). The waves' frequency range follows the structure of the background magnetic field (Figure 3(i)), and these waves' wave normal angles (θ , the angle between the wave normal and the direction of the background magnetic field) are significantly oblique—up to 80° (Figure 3(j)).

The entropy dynamics during a bow shock crossing by MMS on 2017 November 2.

According to, e.g., Landau & Lifshitz (1977), for a state of a system close to thermodynamic equilibrium, assumed to prevail at some distance upstream and downstream of the shock, the

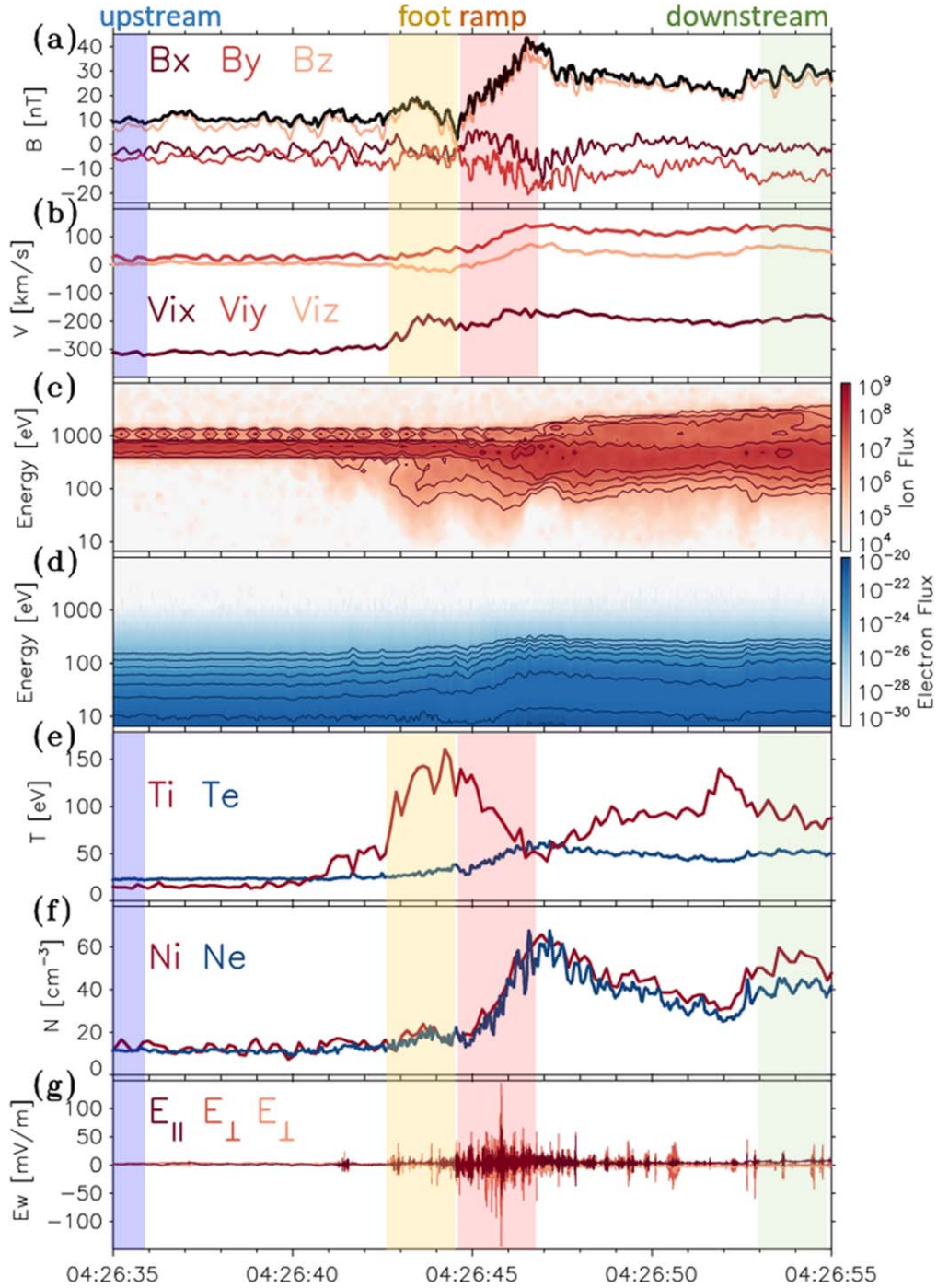


Figure 1. The MMS3 crossing of the bow shock on 2015 November 2: (a) magnetic field dynamics (the components are presented in the GSE coordinate system; the black curve represents the magnetic field magnitude), (b) ion bulk velocity in the GSE coordinate system, (c) ion omni-directional distribution flux (estimated as the second moment of the entire distribution), (d) electron omni-directional flux, (e) electron (blue) and ion (red) temperature, (f) electron (blue) and ion (red) density, and (g) electric perturbations across the shock.

kinetic ensemble entropy $S = -k_B H$ per particle can be given by the expression (Parks et al. 2012)

$$H(\vec{r}) = -\frac{S(\vec{r})}{k_B} = -\int f(\vec{r}, \vec{v}) \cdot \ln(f(\vec{r}, \vec{v})) d^3v,$$

where the integral is over all velocity space, which can change but contains a constant number of particles. We use here the entropy decomposition to the spatial and velocity entropy

components established in (Liang et al. 2019) to proceed with the entropy density $H(\vec{r})$ in the spatial space. $f(\vec{r}, \vec{v})$ can be rewritten in terms of a probability or normalized f function, i.e., $f(\vec{r}, \vec{v}) = N\tilde{f}(\vec{r}, \vec{v})$ with $\int \tilde{f}(\vec{r}, \vec{v}) d^3v = 1$ following (Parks et al. 2012), and will be used below for normalized solid angle distributions with the partial density distribution on energy (the binned energy channel for the spacecraft data, so that N is the density of particles in the

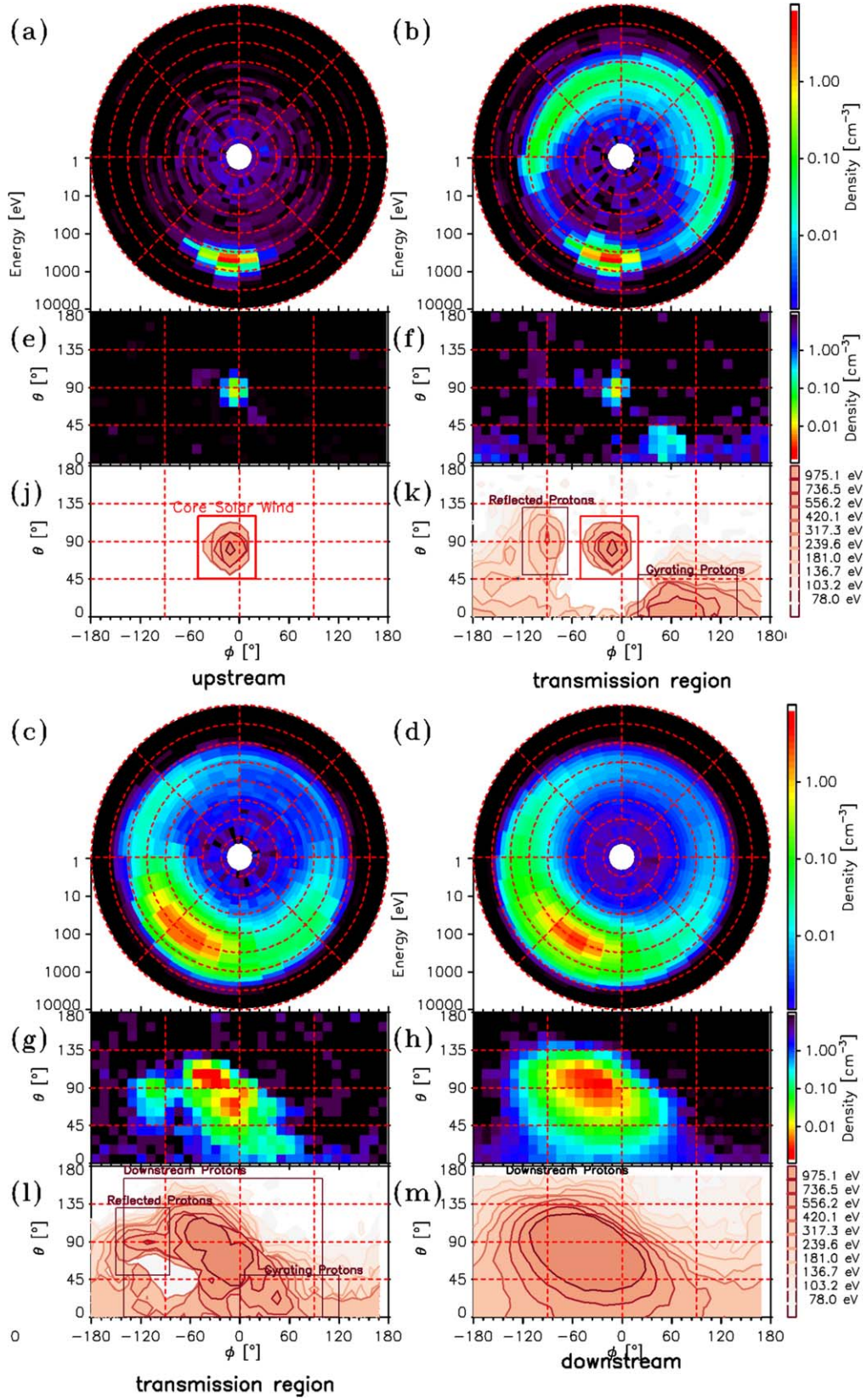


Figure 2. Ion density distributions in the azimuthal angle φ ($\varphi = 0$ corresponds to the anti-sunward radial direction) and the ion energy (the radial axis) domain in the far upstream (a), foot (b), ramp (c), and downstream (d) regions. The polar diagrams of the ion phase space density in the φ - θ domain are presented in panels (e)–(h) for the same shock regions. The sky diagrams in panels (j)–(m) show the directional distribution of the same flux value for the different energies in the φ - θ domain.

channel energy range, and $v^{*2}dv^* \int f \sim (\vec{r}, \vec{v}^*) \sin \theta d\theta d\varphi = 1$, where v^* is the velocity corresponding to the energy channel. The integral for the binned measurements is constrained by the

detector energy channels and then combined into the sky map (32×16 angles resolution in the MMS measurements) and the energy channels the integral becomes a sum decomposed to the

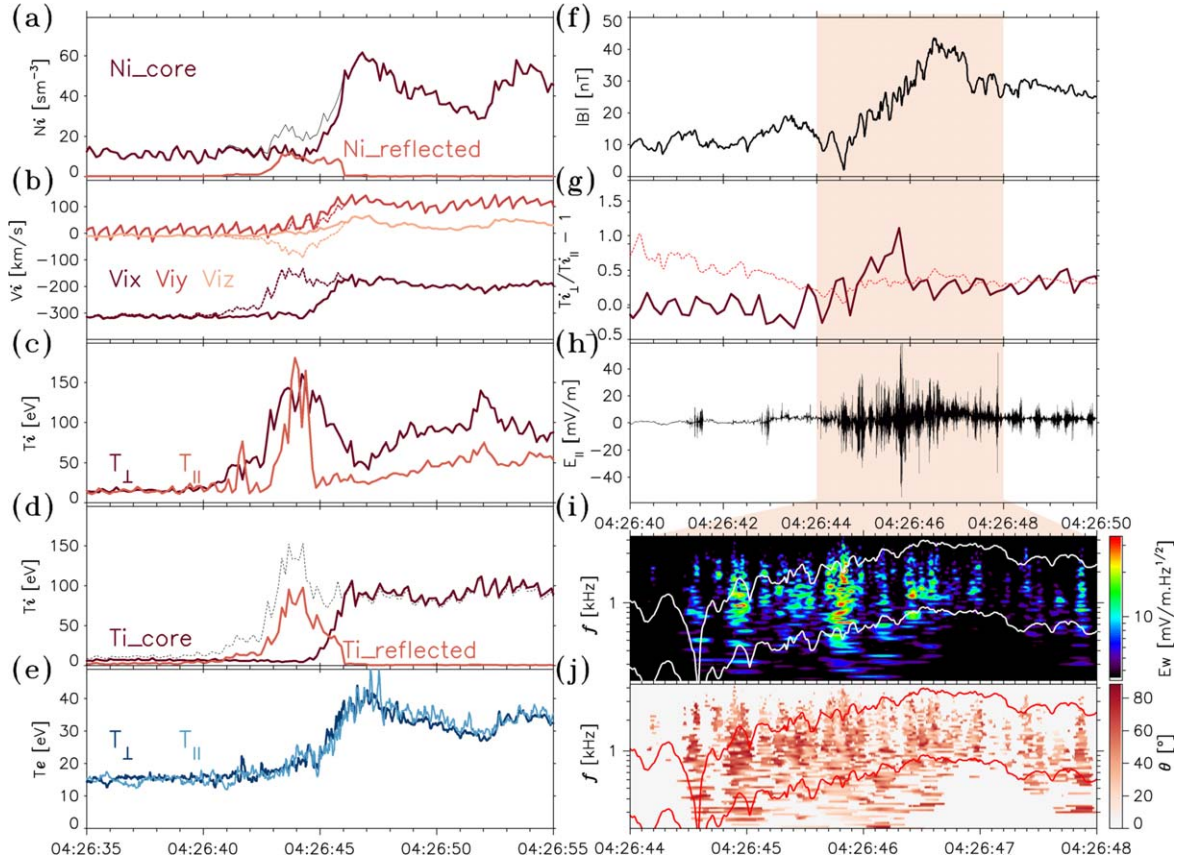


Figure 3. (a) Density of the core ion population and the reflected ion population. (b) Bulk velocity of core population ions (the solid curves); here and in panels (b) and (d) the estimation made from the entire distribution (Figure 1) is shown by the dashed curves. (c) Ion temperatures estimated from the entire distribution, (d) temperatures estimated for the core and ion-reflected populations, (e) electron temperatures: parallel and transverse to the background magnetic field, (f) background magnetic field magnitude, (g) ion anisotropy $A = T_{\perp}/T_{\parallel} - 1$ estimated for the core ion population. The red dashed curve denotes the field perturbation (Figure 1), (i) dynamic spectrum of the electric field perturbation during the interval highlighted in panels (f)–(h) and (j) the wave normal angle of the electrostatic perturbations.

energy channels (i index) and the solid angle bins ($i\theta$, $i\varphi$ indices):

$$\begin{aligned}
 H(\vec{r}) &= -\sum_i \sum_{i\theta, i\varphi} n_i p_{i\theta i\varphi} \ln n_i p_{i\theta i\varphi} v_i^2 \Delta v_i \sin \theta_{i\theta} \Delta \theta \Delta \varphi = \\
 &= -\sum_i n_i \ln n_i v_i^2 \Delta v_i - \sum_i n_i \sum_{i\theta, i\varphi} p_{i\theta i\varphi} \ln p_{i\theta i\varphi} \sin \theta_{i\theta} \Delta \theta \Delta \varphi \\
 H(\vec{r}) &= -\sum_i n_i \ln n_i v_i^2 \Delta v_i - \sum_i n_i h_i,
 \end{aligned}
 \tag{1}$$

where $p_{i\theta i\varphi}$ is the probability of the θ , φ state and n_i is the partial density in the i th energy channel (we mark the components as $A = \sum_i n_i \ln n_i v_i^2 \Delta v_i$ and $B = \sum_i n_i h_i$ with corresponding indices e and p for electrons and protons, respectively). We apply Equation (1) to proceed with the entropy changes across the bow shock crossing by MMS on 2017 November 2, as discussed above. The dynamics of the entropy of the plasma volume going through the shock are shown in Figure 4 for electrons (blue) and ions (red). Figures 4(a) and (c) present the partial density values n_i in the MMS energy channels ($N = \sum_i n_i$) of electrons and protons in the downstream and upstream of the shock (presented in Figures 1 and 3). The partial entropy values h_i are shown in Figure 4 for electrons h_{ei} (b) and protons h_{pi} (d) estimated from the upstream and downstream distribution functions.

The increase in electron density across the shock is concentrated in the energy range of 10–1000 eV (Figure 4(a)). Electrons have almost uniform distribution at all energies, which is reflected in the high and almost equal values of h_{ei} in all the energy channels (Figure 4(b)). This corresponds to much higher electron thermal speed values in comparison with the solar wind bulk velocity. Thus, h_{ei} is close in the upstream and downstream regions, so, the changes in the distribution function do not lead to significant changes in the electron entropy values across the shock.

The proton population experiences significant changes in entropy across the shock. The lower values of the entropy corresponding to the solar wind flow of protons and helium in the upstream evolve to the smoothed distributions with almost 3 times higher values:

1. In the upstream, the almost uniformly randomized fluxes in the wide range of energies below 100 eV and above 2 keV (the light red curve in Figure 4(d)) provide the highest values of the partial entropy values h_{pi} of protons in the upstream. Conversely, the energy channels covering the directed solar wind flow (200–2 keV) have partial proton entropy values ~ 4 –5 times lower, and these values determine the entropy density per particle in the upstream because of much higher statistical weights n_{pi} (Figure 4(c), A_p in Equation (1)).

2. In the downstream, the less anisotropic proton flow distribution has higher partial entropy values h_{pi} in all the energy channels (Figure 4(d)) that together with the spreading of the proton energy spectrum (the dark red curve in

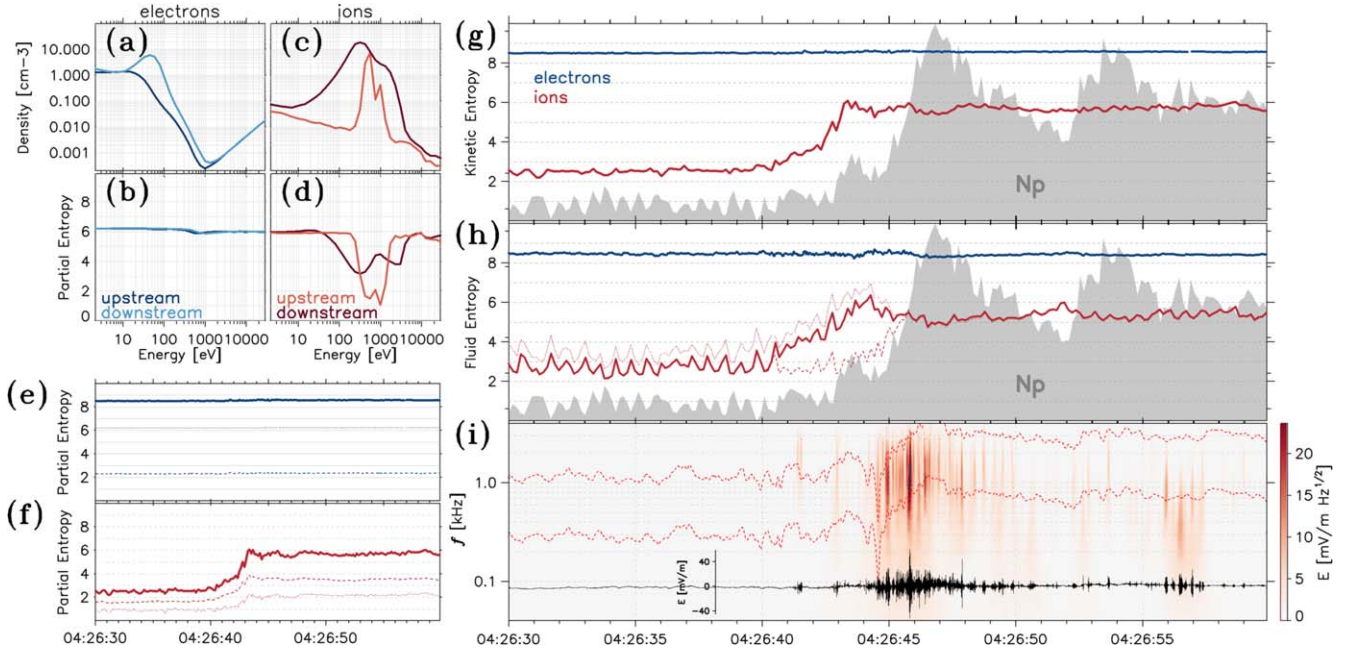


Figure 4. The partial (in the FPI energy channels) electron density (a) and electron partial entropy estimated by the Boltzmann kinetic approach in the upstream (light blue) and downstream (dark blue). The partial proton density (c) and proton partial entropy (d) in the upstream (light red) and downstream (dark red). The dynamics of the entropy of the proton (the red curve) and electron (the blue curve) populations estimated by the Boltzmann kinetic approach (g) and based on the thermodynamic potentials (h). The dotted curve is based on the moments obtained from the full ion distribution function (spoiled by the reflected population) with an enhancement in temperature in the foot region caused by the reflected population, i.e., one needs to process the core and reflected population moments separately. The dashed red curve represents the core population’s jump in entropy, which is coincident with the slowing down of the bulk velocity in the foot and the increase in the ion temperature from the upstream to the downstream (Figure 4(c)). The solid red curve represents the dynamics of the entropy based on the total pressure derived from partial pressures of the core and reflected populations: $p = (n_{\text{cor}}T_{\text{cor}} + n_{\text{ref}}T_{\text{ref}})$. The plasma density is shown by the gray background. The dynamics spectrum of wave electric field perturbations along the background magnetic field direction are shown in panel (k) with the waveform presented by the black curve (the waveform amplitude scale is shown in the bottom right of the panel).

Figure 4(c) is reflected in a 2–3 times increase in the partial entropy per particle.

The dynamics of the partial entropy H (Equation (1)) is presented in Figure 4(e) for electrons and Figure 4(f) for protons. The contributions from the two components are shown by the dashed curve $A = \sum_i n_i \ln n_i v_i^2 \Delta v_i$, and the dotted curve ($B = \sum_i n_i h_i$). These components show the simultaneous increase in both values A_p and B_p for protons in the foot region (Figure 4(f), (g)), where the plasma density is shown in the background) but almost no changes for electrons (Figure 4(e), (g)). In the foot region, the enhancement of entropy is provided by the reflected population. In the ramp, the partial entropy of the core population grows with the increase in plasma temperature and the decrease in bulk flow velocity. The electron entropy density is much higher in the upstream and has an $\sim 2\%$ – 3% increase in the downstream (consistent with the results obtained for this shock crossing by Lindberg et al. 2022), which is, however, about the estimation confidence interval, i.e., electron dynamics are almost adiabatic across this shock.

The fluid (thermodynamic) description allows one to express the total jump in entropy ΔS across the shock by assuming a smooth change from the upstream to the downstream quasi-equilibrium distribution function (see e.g., Serrin 1959; Landau & Lifshitz 1977). Then the jump in the entropy per unit mass at the shock, judged in the respective frames of the bulk plasma flow, is given by

$$\Delta S_{\text{MHD}} = \ln \left[\frac{P_2 \left(\frac{\rho_1}{\rho_2} \right)^{\gamma_a}}{P_1} \right] = k_B \ln \frac{n_1}{n_2} \left(\frac{T_2}{T_1} \right)^{\frac{1}{\gamma_a - 1}},$$

where $\gamma_a = 5/3$ is the adiabatic index, suggesting that particles behave similarly to a monatomic ideal gas with 3 degrees of freedom. This value of $\gamma_a \cong 5/3$ was justified for the bow shock crossings by Lindberg et al. (2022). For this specific choice of γ_a , it follows that a gas, reacting strictly adiabatically at the shock compression, will not increase its thermal entropy. Figure 4(h) presents the thermodynamic approach to the jump in entropy for ions and electrons confirming the results obtained from the kinetic approximation. A similar set of calculations using the measured electron distributions show that the jump in electron entropy across the shock is much less: $\sim 2\%$ – 5% . This demonstrates that the main contribution to the entropy generation is provided by the core ions. Thus, in this case, the downstream electron temperature T_e (where the electron anisotropy is almost zero, and the marginal stability threshold for electron modes is not exceeded anywhere) matches the adiabatic expectation $T_e/T_{e0} = 2 - 2.1$ (here, T_{e0} is the electron upstream temperature). The downstream proton temperature $T/T_{i0} \sim 6 - 6.5$ is much larger than the adiabatic expectation $T/T_{i0} = 2$, so most of the entropy produced by the shock goes to the protons. In analogy to the so-called *magnetic pumping* mechanism (Lichko et al. 2017; Fowler et al. 2020), two basic ingredients are needed for plasma irreversible heating—the presence of a temperature anisotropy, induced by field amplification coupled to adiabatic invariance, and a mechanism to break the adiabatic invariance itself (the local generation of the ion cyclotron waves as can be seen in Figure 4(i)). This confirms that wave-particle interactions dominate the energy dissipation of

collisionless shocks (Wilson et al. 2014) and the numerical results reported by Guo et al. (2017, 2018), which highlight the anisotropy and wave generations to be the key factor for entropy growth across the CS.

2. Discussion

The unprecedented high-time resolution plasma measurements from the four MMS spacecraft provide an opportunity for the detailed evaluation of the plasma dynamics across the front of the CS during multiple crossings of the terrestrial bow shock by MMS in 2015–2018. In the vicinity of the front one can distinguish several ion populations, well known from previous studies, namely, (1) the core ions and (2) the reflected ions, ions mirrored by the electrostatic potential and mirror force from the shock surface almost without a change in energy, (3) gyrating ions, the ions turning around the front several times and gaining energy due to gyrosurfing drift and acceleration, and (4) the ions leaking from the downstream; these ions have a distribution similar to that of the distribution of the partial downstream (the part with the velocity component directed to the Sun), indicating that the source for this population is leakage from the downstream.

Processing different populations separately allows one to evaluate the ion moments (bulk velocity, temperature, etc.) for each population. It shows that the change in the solar wind core population macroscopic parameters begins in the foot region but the main change occurs in the ramp, where its bulk velocity slows down by the electrostatic potential and its temperature significantly increases. The foot region properties are determined by the counter-streaming plasma flows between the upstream plasma and the reflected population. They are manifested by the formation of the temperature peak in the foot region (as can be seen in Figure 1(e)) due to the relative motion of several instantaneously present ion species. The ion reflection at the front of a supercritical quasi-perpendicular shock is essentially non-specular as shown by Gedalin (2016) and Balikhin & Gedalin (2022). As the plasma beta is finite, the turning distances in the foot depend upon the phase of Larmor rotation during the interaction with the shock front and the velocity of a particular ion (Balikhin & Gedalin 2022). During the crossing of the foot region by the spacecraft, the population of reflected ions varies as ions with shorter turning distances are continuously added to it. The results of the ISEE mission have shown that the major ion thermalization occurs in the process of joint gyration of the directly transmitted and reflected ions downstream of the magnetic ramp (Sckopke et al. 1990). Overshoots and undershoots of the magnetic field downstream of the ramp result from such a gyration due to the pressure balance. Ion heating takes place on a spatial scale that corresponds to the scale of the overshoots/undershoots' trail and is significantly larger than the width of the magnetic ramp. The ion proxies based on the solar wind core population reproduce rather well the variations in the electrostatic potential (application of the total integral moments fails to reproduce the potential (Hanson et al. 2019), so the bulk velocity changes are well explained by the electrostatic potential drop in the ramp.

3. Conclusions

The plasma entropy changes significantly from the upstream to the downstream, mostly due to the ions. The analysis of the entropy growth for different ion populations across the front of

the stationary supercritical CS shows that the major growth of the total entropy is related to changes in the core ion population. It occurs in the foot region where the core and reflected ion populations coexist and interact through ion cyclotron wave activity that results in modification of the core ion distribution. In addition, the entropy significantly increases in the ramp following the increase in the ion distribution anisotropy. The major dissipation mechanism consists of the heating of the core ion population. It operates in the foot and ramp regions, and the processes after the ramp play a minor role in the evolution of ion entropy. Little if any change in the electron entropy occurs, and if present, occurs in the vicinity of the ramp. Since current models of electron-ion anomalous resistivity would predict significant entropy increases in both the ions and electrons, these observations demonstrate that the role of the anomalous resistivity that was proposed in early works on CSs is negligible (Galeev 1976; Sagdeev 1966). In other words, *anomalous collisions* between electrons and ions caused by various plasma instabilities do not lead to the stochasticization of an electron population and the irreversibility of the electron dynamics across the shock front. This is in full agreement with the current views that the electron thermalization at the shock front of a supercritical quasi-perpendicular shock is the result of the action of macroscopic magnetic and electric fields within the shock rather than anomalous collisions between electrons and ions due to various instabilities.

To summarize, the analysis of the entropy of ions and electrons populations across stationary supercritical CSs shows that (1) the major growth of the total entropy is related to the core ion population thermalization, (2) ion thermalization starts in the foot (where the core and reflected ion populations coexist and interact through wave activity that modifies the ion core distribution) and finalizes in the ramp (where the core population entropy enhancement is maximal) with the increase in the ion distribution anisotropy, (3) the major dissipation mechanism consists of the anisotropic heating of the core ion population and its simultaneous scattering by the intense ion cyclotron waves, (4) the change in the electron entropy is significantly smaller if any, and (5) this implies that the role of the anomalous resistivity that was proposed in early works on CSs is negligible.

Acknowledgments

O.V.A and V.K. were supported by grants 80NSSC20K0697 and 80NSSC20K0697. O.V.A was supported by NSF grant No. 1914670, NASA's Living with a Star (LWS) program (contract 80NSSC20K0218), and NASA grants Nos. 80NNSC19K0848, 80NSSC22K0433, and 80NSSC22K0522. M. B. acknowledges support by UK STFC grant ST/R000697/1.

ORCID iDs

O. V. Agapitov  <https://orcid.org/0000-0001-6427-1596>
 V. Krasnoselskikh  <https://orcid.org/0000-0002-6809-6219>
 M. Balikhin  <https://orcid.org/0000-0002-8110-5626>
 J. W. Bonnell  <https://orcid.org/0000-0002-0675-7907>
 F. S. Mozer  <https://orcid.org/0000-0002-2011-8140>

References

- Axford, W. I., Leer, E., & Skadron, G. 1977, *ICRC*, **11**, 132
 Balikhin, M., & Gedalin, M. 2022, *ApJ*, **925**, 90
 Bame, S. J., Asbridge, J. R., Gosling, J. T., et al. 1979, *SSRv*, **23**, 75

- Bell, A. R. 1978, [MNRAS](#), **182**, 147
- Burch, J. L., Moore, T. E., Torbert, R. B., & Giles, B. L. 2016, [SSRv](#), **199**, 5
- Bim, J., Raeder, J., Wang, Y. L., Wolf, R. A., & Hesse, M. 2004, [AnGeo](#), **22**, 1773
- Du, S., Zank, G. P., Li, X., & Guo, F. 2020, [PhRvE](#), **101**, 033208
- Ergun, R. E., Tucker, S., Westfall, J., et al. 2016, [SSRv](#), **199**, 167
- Fowler, C. M., Agapitov, O. V., Xu, S., et al. 2020, [GeoRL](#), **47**, e2019GL086408
- Galeev, A. A. 1976, Physics of Solar Planetary Environments: Proc. of the Int. Symp. on Solar-Terrestrial Physics, Vol. I, ed. D. J. Williams (Washington, DC: American Geophysical Union), 464
- Fuselier, S. A., Burch, J. L., Cassak, P. A., et al. 2016, [GeoRL](#), **43**, 1435
- Gedalin, M. 2016, [JGRA](#), **121**, 10,754
- Guo, X., Sironi, L., & Narayan, R. 2017, [ApJ](#), **851**, 134
- Guo, X., Sironi, L., & Narayan, R. 2018, [ApJ](#), **858**, 95
- Halekas, J. S., Poppe, A. R., & McFadden, J. P. 2014, [JGRA](#), **119**, 5133
- Hanson, E. L. M., Agapitov, O. V., Mozer, F. S., et al. 2019, [GeoRL](#), **46**, 2381
- Hanson, E. L. M., Agapitov, O. V., Mozer, F. S., et al. 2020a, [JGRA](#), **125**, e2019JA027231
- Hanson, E. L. M., Agapitov, O. V., Vasko, I. Y., et al. 2020b, [ApJL](#), **891**, L26
- Kennel, C. F., Edmiston, J. P., & Hada, T. 1985, Collisionless Shocks in the Heliosphere: A Tutorial Review, 34 (Washington, DC: American Geophysical Union), 1
- Krasnoselskikh, V., Balikhin, M., Walker, S. N., et al. 2013, [SSRv](#), **178**, 535
- Krymskii, G. F. 1977, [DoSSR](#), **234**, 1306
- Le Contel, O., Leroy, P., Roux, A., et al. 2016, [SSRv](#), **199**, 257
- Landau, L. D., & Lifshitz, E. M. 1977, Quantum Mechanics (Non-Relativistic Theory), 3 (Oxford: Pergamon)
- Leroy, M. M., Winske, D., Goodrich, C. C., Wu, C. S., & Papadopoulos, K. 1982, [JGRA](#), **87**, 5081
- Liang, H., Cassak, P. A., Servidio, S., et al. 2019, [PhPI](#), **26**, 082903
- Lichko, E., Egedal, J., Daughton, W., & Kasper, J. 2017, [ApJL](#), **850**, L28
- Lindberg, M., Vaivads, A., Raptis, S., et al. 2022, [Entrp](#), **24**, 745
- Lindqvist, P.-A., Olsson, G., Torbert, R. B., et al. 2016, [SSRv](#), **199**, 137
- Montgomery, D. C., & Tidman, D. A. 1964, [A&A](#), **579**, A13
- Liu, Y., Richardson, J. D., Belcher, J. W., & Kasper, J. C. 2007, [ApJ](#), **659**, L65
- Park, J., Caprioli, D., & Spitkovsky, A. 2015, [PhRvL](#), **114**, 085003
- Parks, G. K., Lee, E., McCarthy, M., et al. 2012, [PhRvL](#), **108**, 061102
- Pollock, C., Moore, T., Jacques, A., et al. 2016, [SSRv](#), **199**, 331
- Russell, C. T., Anderson, B. J., Baumjohann, W., et al. 2016, [SSRv](#), **199**, 189
- Sagdeev, R. Z. 1966, [RvPP](#), **4**, 23
- Schwartz, S. J., Goodrich, K. A., Wilson, L. B., III, et al. 2022, [JGRA](#), **127**, e2022JA030637
- Schwartz, S. J., Henley, E., Mitchell, J., & Krasnoselskikh, V. 2011, [PhRvL](#), **107**, 215002
- Schwartz, S. J., Kucharek, H., Farrugia, C. J., et al. 2021, [GeoRL](#), **48**, e2020GL091859
- Schwartz, S. J., Thomsen, M. F., Bame, S. J., & Stansberry, J. 1988, [JGRA](#), **93**, 12923
- Skopke, N. 1995, [AdSpR](#), **15**, 261
- Skopke, N., Paschmann, G., Brinca, A. L., Carlson, C. W., & Lühr, H. 1990, [JGRA](#), **95**, 6337
- Serrin, J. 1959, Fluid Dynamics I (Encyclopedia of Physics), Vol. 3 (Berlin, Heidelberg: Springer), 125
- Vink, J., Broersen, S., Bykov, A., & Gabici, S. 2015, [A&A](#), **579**, A13
- Wilson, L. B., Goodrich, K. A., Turner, D. L., et al. 2022, [FrASS](#), **9**, 369
- Wilson, L. B., III, Sibeck, D. G., Breneman, A. W., et al. 2014, [JGRA](#), **119**, 6475
- Yang, Z., Liu, Y. D., Parks, G. K., et al. 2014, [ApJL](#), **793**, L11